

# Cooperative photoinduced metastable phase control in strained manganite films

Jingdi Zhang<sup>1,2\*</sup>, Xuelian Tan<sup>3</sup>, Mengkun Liu<sup>1,4</sup>, S. W. Teitelbaum<sup>5</sup>, K. W. Post<sup>1</sup>, Feng Jin<sup>3</sup>, K. A. Nelson<sup>5</sup>, D. N. Basov<sup>1</sup>, Wenbin Wu<sup>3,6</sup> and R. D. Averitt<sup>1,2\*</sup>

**A major challenge in condensed-matter physics is active control of quantum phases<sup>1,2</sup>. Dynamic control with pulsed electromagnetic fields can overcome energetic barriers, enabling access to transient or metastable states that are not thermally accessible<sup>3–5</sup>. Here we demonstrate strain-engineered tuning of  $\text{La}_{2/3}\text{Ca}_{1/3}\text{MnO}_3$  into an emergent charge-ordered insulating phase with extreme photo-susceptibility, where even a single optical pulse can initiate a transition to a long-lived metastable hidden metallic phase. Comprehensive single-shot pulsed excitation measurements demonstrate that the transition is cooperative and ultrafast, requiring a critical absorbed photon density to activate local charge excitations that mediate magnetic–lattice coupling that, in turn, stabilize the metallic phase. These results reveal that strain engineering can tune emergent functionality towards proximal macroscopic states to enable dynamic ultrafast optical phase switching and control.**

Precision tuning of the local environment in complex materials provides a route to control macroscopic functionality, thereby offering a glimpse into how microscopic interactions conspire towards emergent behaviour. Static tuning can be achieved through doping, heterostructuring, or epitaxial strain. Dynamic tuning can be achieved with electromagnetic fields, which includes photoexcitation<sup>1,2</sup>. Dynamic tuning examples include the melting of stripe order in a high- $T_c$  cuprate in favour of superconductivity, the generation of a hidden phase in a layered dichalcogenide, and the observation of Floquet states in a topological insulator<sup>3–5</sup>. Transition-metal oxides are of considerable interest with regards to dynamic tuning because of structure–function coupling arising, predominantly, from octahedral rotations and distortions<sup>6–8</sup>. The rich structure–function coupling results in a complex energy landscape with distinct optical signatures that facilitate identification of dynamic phase changes<sup>9,10</sup>. Doped rare-earth perovskite manganites, derived from the Mott-insulating parent compound  $\text{ReMnO}_3$  ( $\text{Re} = \text{Pr}, \text{La}, \text{Nd}$ ), have proven fertile in the search for novel dynamics, with a focus on the insulator-to-metal transition (IMT)<sup>11–15</sup>, which is strongly influenced from coupling between the lattice and the underlying electronic and magnetic structure<sup>16–19</sup>.

An important path forward that has not been explored is static tuning of the initial state from which photoexcitation proceeds, providing considerable flexibility to explore and ultimately control the energy landscape from which novel macroscopic states emerge. We have utilized elastic strain engineering through epitaxial growth<sup>20,21</sup> to hide the low-temperature ferromagnetic metallic (FM)

phase present in unstrained  $\text{La}_{2/3}\text{Ca}_{1/3}\text{MnO}_3$  (LCMO,  $T_c \approx 260\text{ K}$ ) in favour of an antiferromagnetic insulating (AFI) phase<sup>22,23</sup> utilizing the anisotropic strain from  $\text{NdGaO}_3$  (001) substrates (see Supplementary Information). The strain-induced AFI phase originates from enhanced orthorhombicity of the LCMO lattice, where octahedral tilting and strain-enhanced Jahn–Teller-like distortion break the cubic symmetry, decreasing the Mn–O–Mn bond angle. This suppresses the ferromagnetism and  $d$ -electron itinerancy, resulting in a low-temperature charge-ordered insulating state that evolves towards the conventional paramagnetic insulating phase at higher temperatures. As we detail below, a long-lived metastable FM phase is recovered upon photoexcitation, demonstrating a remarkable level of control of the photoinduced IMT.

Figure 1a shows resistivity measurements for a strained 30 nm LCMO film. In zero applied magnetic field, the film remains insulating at all temperatures (due to strain-enhanced orthorhombicity<sup>22,23</sup>, as depicted in Fig. 1b). For fields above 3 T, the insulating phase collapses, becoming a ferromagnetic metal at low temperatures. Figure 1c details the phase diagram of strained LCMO as determined from the field-dependent transport measurements<sup>22,23</sup>. The FM and AFI phases coexist over the range from 0 to 3 T, depending on temperature. To characterize the time-integrated electrodynamic response of the strained films, the optical conductivity was measured from 100 meV to 5 eV using spectroscopic ellipsometry (Fig. 1d). With decreasing temperature, the film displays spectral weight transfer from a small polaron ( $\sim 1.5\text{ eV}$ ) peak to a sharp well-defined peak (1.7 eV), suggestive of charge order and associated with intersite transitions  $\text{Mn}^{3+}\text{–Mn}^{4+}$  ( $d_1^3 d_j^4 \rightarrow d_1^4 d_j^3$ ), as depicted in Fig. 1e<sup>24–27</sup>. This is in stark contrast to the development of a coherent Drude response with decreasing temperature in unstrained films (Supplementary Fig. 3a).

As we now show, photoexcitation recovers the hidden FM phase of the strain-engineered insulating LCMO films. The films were excited with 1.55 eV photon energy pulses (35 fs, see Supplementary Information for details) resonantly exciting intersite  $\text{Mn}^{3+}\text{–Mn}^{4+}$  transitions (Fig. 1d,e). Terahertz (THz) time domain spectroscopy was used to measure the photoinduced change in conductivity. The photoinduced phase transition from the insulating state to the ‘hidden’ ferromagnetic metallic state is shown in Fig. 2, and constitutes the main result of this work. In the absence of photoexcitation, there is no measurable THz conductivity, consistent with an insulating state and the optical conductivity measurements in Fig. 1d. In Fig. 2, the temperature of the LCMO is decreased from 120 K to 80 K in

<sup>1</sup>Department of Physics, University of California at San Diego, La Jolla, California 92093, USA. <sup>2</sup>Department of Physics, Boston University, Boston, Massachusetts 02215, USA. <sup>3</sup>Hefei National Laboratory for Physical Sciences at Microscale, and High Magnetic Field Laboratory of Chinese Academy of Sciences, University of Science and Technology of China, Hefei, Anhui 230026, China. <sup>4</sup>Department of Physics, Stony Brook University, Stony Brook, New York 11790, USA. <sup>5</sup>Department of Chemistry, Massachusetts Institute of Technology, Cambridge, Massachusetts 02139, USA. <sup>6</sup>Collaborative Innovation Center of Advanced Microstructure, Nanjing 210093, China. \*e-mail: [jdzhang@physics.ucsd.edu](mailto:jdzhang@physics.ucsd.edu); [raveritt@ucsd.edu](mailto:raveritt@ucsd.edu)

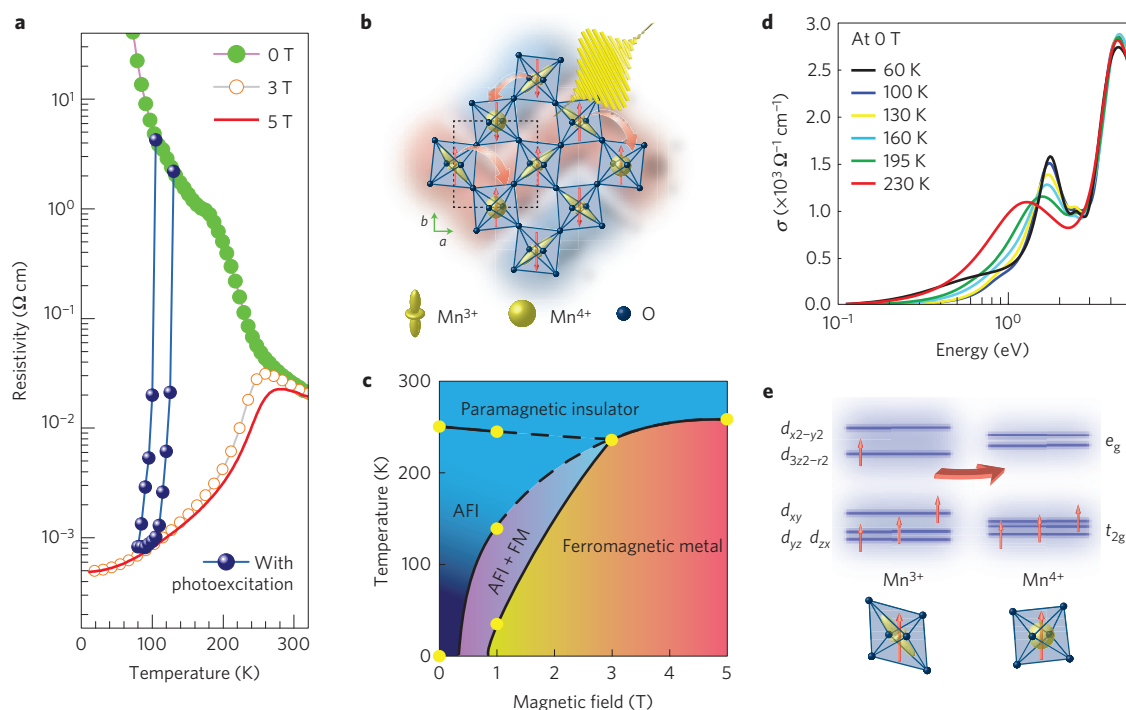


**Figure 1 | Strain engineered  $\text{La}_{2/3}\text{Ca}_{1/3}\text{MnO}_3$  (LCMO) thin film.** **a**, d.c. resistivity-temperature curves for a 30 nm strain-engineered LCMO film, under various magnetic fields (0–5 T). The blue dots are the conductivity following excitation with sub-50 fs 1.5 eV pulses under zero field (see main text and Fig. 2). **b**, Depiction of a strain-engineered LCMO lattice, where the dashed rectangle represents the enhanced orthorhombic unit cell in the  $a$ - $b$  plane. **c**, Phase diagram of a sample film, where boundaries (AFI, antiferromagnetic insulator; FM, ferromagnetic metal) are extrapolated from magnetization and resistivity measurements (yellow dots). **d**, Optical conductivity ( $\sigma$ ) of the film at various temperatures, showing a resonance peak at  $\sim 1.7$  eV, corresponding to intersite hopping of  $d$  electrons ( $\text{Mn}^{3+} \rightarrow \text{Mn}^{4+}$ ). **e**, Schematic of photoexcited intersite transitions of the Mn  $d$  electrons. The  $\text{Mn}^{3+}$   $e_g$  electrons can be excited to the empty orbital of  $\text{Mn}^{4+}$  ions (see also red arrows in **b**).

5 K decrements. Two measurements of THz conductivity, before and after 1.55 eV photoexcitation (fluence  $\sim 2 \text{ mJ cm}^{-2}$ ), were performed at each temperature of the cooling process. At temperatures lower than 105 K, a persistent change of THz conductivity occurs after photoexcitation. When the sample was cooled by a further 5 K (in the absence of photoexcitation), the conductivity remained constant, and increased only upon additional photoexcitation. The conductivity continued to increase, forming a step-like curve as a function of decreasing temperature, until it reached the full metallic state conductivity of  $\sim 1,200 \Omega^{-1} \text{ cm}^{-1}$  at 80 K. Subsequently, the conductivity was measured with increasing temperature in the absence of photoexcitation. A monotonic decrease was observed, with a return to the insulating state at 130 K. After finishing the thermal cycle, the THz conductivity was measured without any optical excitation. The LCMO film again remained insulating at all temperatures. The entire process could be repeated without permanent changes in the optical properties of the film.

The photoinduced THz conductivity (PTC) is stable as long as the temperature is maintained. Further, the maximum conductivity is the same value as obtained with a strong magnetic field. This is clear from the blue dots of Fig. 1a, where the PTC from Fig. 2 is mapped onto the temperature-dependent d.c. resistivity curve. That is, optical excitation results (at 80 K) in a metallic state conductivity equivalent to that accessed with magnetic fields higher than 3 T. The correspondence of the metallic state, obtained through two different pathways, is indicative of dynamic coupling between the charge, spin, and lattice degrees of freedom. The observed laser-induced IMT is a nonequilibrium dynamical process, and not simply laser heating, since the metallic phase is not thermally accessible. In fact, laser heating drives the film back towards the insulating phase.

To further investigate the nature of the photoinduced metastable metallic state, single-shot experiments were performed where, on a

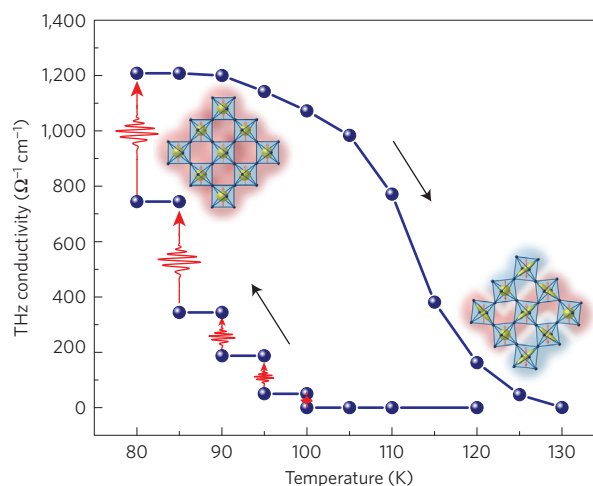


**Figure 2 | Photoinduced insulator-to-metal phase transition in strain-engineered thin film.** With decreasing temperature, photoexcitation (sub-50 fs 1.5 eV pulses at a fluence of  $2 \text{ mJ cm}^{-2}$ ) yields a step-like conductivity progression, until it achieves a conductivity of  $1,200 (\Omega^{-1} \text{ cm}^{-1})$  at 80 K, corresponding to the full ‘hidden’ metallic state. This is more clearly shown in Fig. 1a, with the photoexcitation data plotted as blue dots. Hence, photoexcitation (in zero applied magnetic field) stabilizes the ferromagnetic metallic phase. With increasing temperature (without photoexcitation), the conductivity returns to the insulating phase at 130 K.

shot-by-shot basis, the conductivity change was measured (details in Supplementary Information). Figure 3a plots the resistivity (as determined from the THz probe) as a function of the

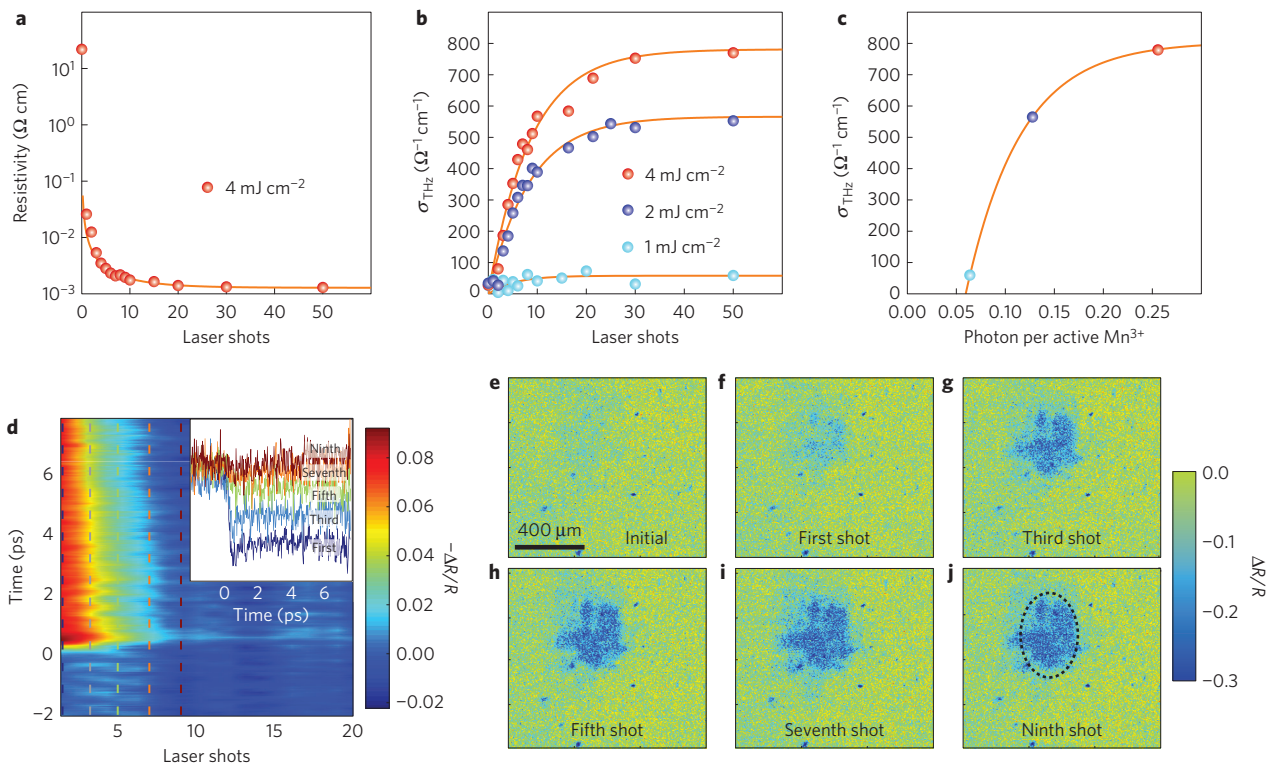


**Figure 3 | Pulse-to-pulse conductivity changes and single-shot dynamics.** **a**, Pulse-to-pulse resistivity change of  $\text{La}_{2/3}\text{Ca}_{1/3}\text{MnO}_3$  film at 80 K, pulse fluence  $4 \text{ mJ cm}^{-2}$ . **b**, Fluence-dependent ( $1\text{--}4 \text{ mJ cm}^{-2}$ ) pulse-to-pulse conductivity ( $\sigma_{\text{THz}}$ , solid lines) saturates to different final conductivity values, indicative of a cooperative effect dependent on the excitation density. **c**, Saturated photoinduced THz conductivity as a function of the average number of photons absorbed per active  $\text{Mn}^{3+}$  atom. The colours correspond to the different intensities in **b**. **d**, Ultrafast pulse-to-pulse reflectivity change dynamics ( $\Delta R/R$ ) at 1.7 eV following 1.5 eV excitation. The inset shows the switching dynamics at selected laser shots, which are line cuts of the 2D plot with the corresponding colours of the dashed lines. **e–j**, The corresponding pulse-to-pulse optical image in the photoinduced metastable metallic state (colour scale denotes the normalized photoinduced reflectivity change in visible spectral range). Dashed ellipse in **j** indicates the full-width at half-maximum of the Gaussian beam.

number of absorbed pulses at 80 K with a fluence of  $4 \text{ mJ cm}^{-2}$ . Following the absorption of the first pulse, the resistivity decreases by approximately three orders of magnitude. With subsequent pulses, the resistivity continues to decrease by a further order of magnitude, reaching a minimum after  $\sim 20$  pulses. Figure 3b plots the photoinduced conductivity versus shot number for different fluences. The  $4 \text{ mJ cm}^{-2}$  (same data as Fig. 3a) saturates at  $800 \Omega^{-1} \text{ cm}^{-1}$ , while at lower fluences the conductivity saturates at a lower value. This is important, showing that the conductivity change does not simply arise from the number of absorbed photons. If there were a simple dependence on the number of absorbed photons, the data at lower fluences would saturate to the same conductivity value as the higher fluence data after a sufficient number of pulses. This is clearly not the case, and indicates a cooperative process with a photon-absorption threshold. Figure 3c plots the conductivity plateaus from Fig. 3b versus the number of absorbed photons (as determined from the fluence and optical conductivity data), yielding a threshold of approximately 0.06 photons per active  $\text{Mn}^{3+}$  to stabilize the metallic phase.

The photoinduced conductivity can take on a range of values, indicating FM and AFI phase coexistence, where photon absorption results in spectral weight transfer from the visible to the far infrared, corresponding to an increase of the FM volume fraction at the expense of the AFI volume fraction. Using effective medium theory (see Supplementary Information) we have determined for different fluences the rate of increase (per laser pulse absorbed) of the FM volume fraction. From this analysis, exponential growth (see equation (6), Supplementary Information) of the FM conductivity is expected, with the resultant fits shown (solid lines) in Fig. 3b.

Starting from the AFI state, the first absorbed pulse drives the LCMO films beyond the percolation threshold, with subsequent pulses further increasing the metallic volume fraction.

Measuring the conductivity dynamics of the pristine AFI state following single-pulse excitation would provide insight into the photoinduced IMT, but is not experimentally feasible on a shot-to-shot basis. Instead, we employed an all-optical single-shot ultrafast spectroscopic method<sup>28</sup>, which faithfully represents the conductivity dynamics because of the aforementioned spectral weight transfer. Figure 3d shows the results of single-shot photoinduced reflectivity dynamics ( $\Delta R/R$ ) probing at the peak of the intersite transition (1.7 eV) following 1.55 eV excitation. There is a decrease in  $\Delta R/R$ , consistent with dynamic spectral weight transfer to THz frequencies, and the IMT dynamics occur on a sub-picosecond timescale, with no evidence of longer timescale dynamics. This is consistent with an ultrafast nonthermal cooperative process driving the IMT. We have also monitored the spatial evolution of photoinduced metallic phase on a shot-to-shot basis (Fig. 3e–j), by taking optical images of the photoexcited area with the laser pulse focused to  $350 \mu\text{m}$  (full-width at half-maximum) in diameter, indicated by the dashed circle. The optical reflectivity of the switched region shows a spatial dependence, due to the Gaussian beam intensity profile, with the highest fluence at its centre. Interestingly, even at the excitation centre, the images clearly show the coexistence of micrometre-scale regions with different reflectivity, consistent with phase coexistence.

We now consider how photoexcitation initiates the dynamics that result in a stabilized metallic phase. Photon absorption at 1.55 eV delocalizes the  $e_g d$ -electrons of the  $\text{Mn}^{3+}$  atoms (Fig. 1b,e and Supplementary Fig. 8) and drives, because of strong electron–phonon

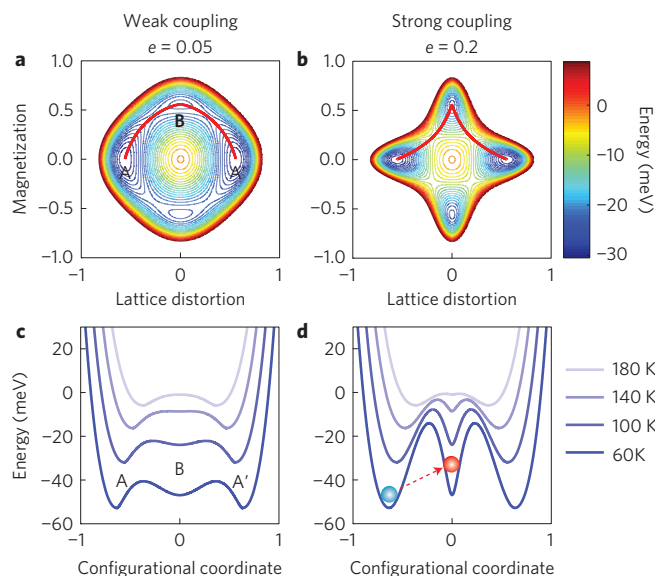


**Figure 4 | Ginzburg-Landau free-energy phenomenology.** **a, b**, Contour plot of the free energy with increasing coupling strength at 100 K, with the form  $F = aQ^2 + bQ^4 + cM^2 + dM^4 + eM^2Q^2$ , where  $Q$  is the lattice distortion,  $M$  the magnetization,  $a = a_0(T - T_{CO})$ , and  $c = c_0(T - T_m)$ , with  $T_{CO}$  and  $T_m$  the charge ordering and ferromagnetic ordering temperatures, respectively. The quantity  $e$  is the magnetic-lattice coupling between the order parameters  $Q$  and  $M$ . A case of weak coupling ( $e = 0.05$ ) is shown in **a** and a case of strong coupling ( $e = 0.2$ ) is shown in **b**. **c, d**, Line sections along the red lines (A-B-A') in **a** and **b**, respectively, at various temperatures. The blue ball, red arrow and red ball depict the transition to a metastable state.

coupling, preferential relaxation of the Jahn-Teller distortions of the  $\text{MnO}_6$  octahedra. This can happen within a fraction of a phonon period, consistent with the ultrafast dynamics observed in the single-shot measurements. In turn, the rapid lattice reorientation directly affects the value of the exchange integral, leading to a transition from antiferromagnetic to ferromagnetic, which can, in principle, preserve the itinerancy of  $d$  electrons in the  $e_g$  band and the relaxed lattice structure<sup>29</sup>, due to the strong magnetic-lattice coupling. However, at low fluences, only a small portion of the  $e_g$   $d$ -electrons delocalize, and the corresponding density of relaxed octahedra is low, hindering the onset of a global phase transition. At higher pump fluences, the population of transiently relaxed octahedra increases such that above  $\sim 0.06$  photons per active  $\text{Mn}^{3+}$  the metallic state is favoured. We note that the PTC shows a strong dependence on the excitation pulse duration. In particular, single-shot measurements (fluence  $2 \text{ mJ cm}^{-2}$ ) with pulse durations from 50 to 200 fs revealed a monotonic decrease in the amplitude of the PTC, with durations greater than 200 fs leading to negligible conductivity changes. This further indicates that the PTC is mediated by coherence effects (that is, dispersive excitation of optical phonons).

Phenomenological Ginzburg-Landau modelling (see Supplementary Information) suggests that magnetic-lattice (ML) coupling<sup>30</sup> is a crucial ingredient to obtain a metastable FM phase that persists over a well-defined range of temperatures in the absence of any sustained external influence. This is shown in Fig. 4, which plots the free energy for the case of weak and strong coupling between the lattice and the magnetization order parameters. In the limit of weak ML coupling (Fig. 4a,c), distinct minima can exist for the lattice-distorted state (A) and the ferromagnetically ordered state (B). A photoexcited trajectory going from A to B as described above is feasible. However, the shallow minimum of the metallic ferromagnetic state would, from thermal fluctuations, result in a rapid return to the lattice-distorted insulating phase. With increasing ML coupling, as depicted in Fig. 4b,d, the magnetic

order has a deeper local minimum, protecting it from thermal fluctuations over an increased temperature range. This suggests that strong ML coupling plays a crucial role in establishing a robust, yet metastable, ferromagnetic metallic state. Nonetheless, biquadratic ML coupling is insufficient to explain all of the features of our data. For example, phase separation may arise from bilinear coupling between orthorhombic and Jahn-Teller distortions, that is, acoustic and optic phonon coordinates<sup>17</sup>. A more complete description of the photoinduced IMT would need to include this in addition to ML coupling.

Our results suggest that strain engineering of transition-metal oxides to precisely control the atomic lattice provides a powerful approach to encode new emergent electronic phases that are robust yet extremely sensitive to dynamic perturbation with optical excitation. This opens a route to design functional optoelectronic devices where the tunable macroscopic properties derive from strongly interacting degrees of freedom present in transition-metal oxides.

## Methods

Methods and any associated references are available in the online version of the paper.

Received 9 September 2015; accepted 10 June 2016; published online 11 July 2016

## References

- Nasu, K. *Photoinduced Phase Transitions* (World Scientific, 2004).
- Zhang, J. & Averitt, R. D. Dynamics and control in complex transition metal oxides. *Annu. Rev. Mater. Res.* **44**, 19–43 (2014).
- Fausti, D. *et al.* Light-induced superconductivity in a stripe-ordered cuprate. *Science* **331**, 189–191 (2011).
- Stojchevska, L. *et al.* Ultrafast switching to a stable hidden quantum state in an electronic crystal. *Science* **344**, 177–180 (2014).
- Wang, Y. H., Steinberg, H., Jarillo-Herrero, P. & Gedik, N. Observation of Floquet-Bloch states on the surface of a topological insulator. *Science* **342**, 453–457 (2013).
- Rondinelli, J. M., May, S. J. & Freeland, J. W. Control of octahedral connectivity in perovskite oxide heterostructures: an emerging route to multifunctional materials discovery. *MRS Bull.* **37**, 261–270 (2012).
- Imada, M., Fujimori, A. & Tokura, Y. Metal-insulator transitions. *Rev. Mod. Phys.* **70**, 1039–1263 (1998).
- May, S. J. *et al.* Quantifying octahedral rotations in strained perovskite oxide films. *Phys. Rev. B* **82**, 14110 (2010).
- Liu, M. *et al.* Terahertz-field-induced insulator-to-metal transition in vanadium dioxide metamaterial. *Nature* **487**, 345–348 (2012).
- Rini, M. *et al.* Control of the electronic phase of a manganite by mode-selective vibrational excitation. *Nature* **449**, 72–74 (2007).
- Miyano, K., Tanaka, T., Tomioka, Y. & Tokura, Y. Photoinduced insulator-to-metal transition in a perovskite manganite. *Phys. Rev. Lett.* **78**, 4257–4260 (1997).
- Takubo, N. *et al.* Persistent and reversible all-optical phase control in a manganite thin film. *Phys. Rev. Lett.* **95**, 017404 (2005).
- Ichikawa, H. *et al.* Transient photoinduced 'hidden' phase in a manganite. *Nature Mater.* **10**, 101–105 (2011).
- Asamitsu, A., Tomioka, Y., Kuwahara, H. & Tokura, Y. Current switching of resistive states in magnetoresistive manganites. *Nature* **388**, 50–52 (1997).
- Li, T. *et al.* Femtosecond switching of magnetism via strongly correlated spin-charge quantum excitations. *Nature* **496**, 69–73 (2013).
- Hwang, H. Y., Cheong, S.-W., Radaelli, P. G., Marezio, M. & Batlogg, B. Lattice effects on the magnetoresistance in doped  $\text{LaMnO}_3$ . *Phys. Rev. Lett.* **75**, 914–917 (1995).
- Ahn, K., Lookman, T. & Bishop, A. Strain-induced metal-insulator phase coexistence in perovskite manganites. *Nature* **804**, 401–404 (2004).
- Burgy, J., Moreo, A. & Dagotto, E. Relevance of cooperative lattice effects and stress fields in phase-separation theories for CMR manganites. *Phys. Rev. Lett.* **92**, 097202 (2004).
- Kiryukhin, V. *et al.* An X-ray-induced insulator-metal transition in a magnetoresistive manganite. *Nature* **386**, 813–815 (1997).
- Chakhalian, J., Millis, A. J. & Rondinelli, J. Whither the oxide interface. *Nature Mater.* **11**, 92–94 (2012).
- Nakamura, M., Ogimoto, Y., Tamaru, H., Izumi, M. & Miyano, K. Phase control through anisotropic strain in  $\text{Nd}_{0.5}\text{Sr}_{0.5}\text{MnO}_3$  thin films. *Appl. Phys. Lett.* **86**, 182504 (2005).

22. Huang, Z. *et al.* Tuning the ground state of  $\text{La}_{0.67}\text{Ca}_{0.33}\text{MnO}_3$  films via coherent growth on orthorhombic  $\text{NdGaO}_3$  substrates with different orientations. *Phys. Rev. B* **86**, 014410 (2012).
23. Wang, L. F. *et al.* Annealing assisted substrate coherency and high-temperature antiferromagnetic insulating transition in epitaxial  $\text{La}_{0.67}\text{Ca}_{0.33}\text{MnO}_3/\text{NdGaO}_3$  (001) films. *AIP Adv.* **3**, 52106 (2013).
24. Basov, D. N., Averitt, R. D., van der Marel, D., Dressel, M. & Haule, K. Electrodynamics of correlated electron materials. *Rev. Mod. Phys.* **83**, 471–541 (2011).
25. Kovaleva, N. *et al.* Spin-controlled Mott–Hubbard bands in  $\text{LaMnO}_3$  probed by optical ellipsometry. *Phys. Rev. Lett.* **93**, 147204 (2004).
26. Quijada, M., Černe, J., Simpson, J. & Drew, H. Optical conductivity of manganites: crossover from Jahn–Teller small polaron to coherent transport in the ferromagnetic state. *Phys. Rev. B* **58**, 16093–16102 (1998).
27. Kim, K., Lee, S., Noh, T. & Cheong, S.-W. Charge ordering fluctuation and optical pseudogap in  $\text{La}_{1-x}\text{Ca}_x\text{MnO}_3$ . *Phys. Rev. Lett.* **88**, 167204 (2002).
28. Shin, T., Wolfson, J. W., Teitelbaum, S. W., Kandyla, M. & Nelson, K. A. Dual echelon femtosecond single-shot spectroscopy. *Rev. Sci. Instr.* **85**, 83115 (2014).
29. Wall, S., Prabhakaran, D., Boothroyd, A. & Cavalleri, A. Ultrafast coupling between light, coherent lattice vibrations, and the magnetic structure of semicovalent  $\text{LaMnO}_3$ . *Phys. Rev. Lett.* **103**, 097402 (2009).
30. Chatterji, T., Henry, P. & Ouladdiaf, B. Neutron diffraction investigation of the magneto-elastic effect in  $\text{LaMnO}_3$ . *Phys. Rev. B* **77**, 212403 (2008).

## Acknowledgements

R.D.A. and J.Z. acknowledge support from DOE—Basic Energy Sciences under Grant No. DE-FG02-09ER46643. X.T., F.J. and W.W. acknowledge support from the NSF of China (Grant No. 11274287), the National Basic Research Program of China (Grant Nos. 2012CB927402 and 2015CB921201) and from NSF of China (Grant Nos. 11474263 and U1432251). S.W.T. and K.A.N. acknowledge support from Office of Naval Research (N00014-12-1-0530) and the National Science Foundation (CHE-1111557). M.L., K.W.P. and D.N.B. are supported by DE-SC0012375 and DE-SC0012592. D.N.B. is the Moore Foundation Investigator in Quantum Materials, EPiQS Initiative GBMF4533.

## Author contributions

J.Z. and R.D.A. developed the idea. X.T., F.J. and W.W. performed material growth and film characterization. J.Z., M.L., K.W.P. and D.N.B. performed the optical conductivity measurements. J.Z., and S.W.T., R.D.A., K.A.N. performed the THz and single-shot measurements. J.Z. and R.D.A. performed the Ginzburg–Landau analysis. R.D.A., W.W., D.N.B. and K.A.N. supervised the project. J.Z. and R.D.A. wrote the paper. All authors contributed to the understanding of the physics and revised the paper.

## Additional information

Supplementary information is available in the [online version of the paper](#). Reprints and permissions information is available online at [www.nature.com/reprints](http://www.nature.com/reprints). Correspondence and requests for materials should be addressed to J.Z. or R.D.A.

## Competing financial interests

The authors declare no competing financial interests.

## Methods

**Thin film sample growth.**  $\text{La}_{2/3}\text{Ca}_{1/3}\text{MnO}_3$  films with thicknesses of 15 and 30 nm were grown on  $\text{NdGaO}_3$  (001) substrates by pulsed laser deposition, using a 248 nm KrF excimer laser with a laser energy density of  $2 \text{ J cm}^{-2}$  and a frequency of 5 Hz. The temperature and oxygen pressure during the deposition were set at  $735^\circ\text{C}$  and 40 Pa, respectively. To optimize the oxygen content and to enhance the epitaxial strain coherence, the films were *ex situ* annealed at  $780^\circ\text{C}$  in a flowing  $\text{O}_2$  atmosphere for 6 h. The structures of the films were analysed by X-ray diffraction using  $\text{Cu-K}\alpha$  ( $\lambda = 1.5406 \text{ \AA}$ , Panalytical X'Pert) radiation, including high-resolution off-specular X-ray reciprocal space mapping measurements at the (116) reflection. The surface morphologies of the films were characterized using atomic force microscopy (Veeco, MultiMode V). The resistivity measurements were performed on a Quantum Design physical property measurement system using a standard four-probe technique.

**Optical conductivity characterization.** The optical conductivity of the LCMO thin films is obtained from the complex dielectric function  $\tilde{\epsilon}(\omega)$  determined by variable angle spectroscopic ellipsometry (VASE). These measurements were performed using two commercial Woollam ellipsometers (IR-VASE and UV-VASE) equipped with in-house-built ultrahigh vacuum cryogenic chambers, covering a wide photon energy range (0.1–5 eV). The mid-infrared to near-infrared (0.05–0.7 eV) spectra was measured using an IR-VASE system based on a Michelson interferometer (Bruker 66 v/S). The near-infrared to ultraviolet (0.6–6 eV) ellipsometry was performed using a VASE system based on a grating monochromator (Woollam HS-190). Both systems work under an ultrahigh vacuum environment from 20 to 400 K.

**THz conductivity measurements.** The output of a 1 kHz, 3 W, 35 fs Ti:sapphire regenerative amplifier (Spectra-Physics Spitfire Pro XP) is used to provide 1.55 eV excitation pulses and generate single-cycle THz pulses by optical rectification in a

ZnTe crystal. We use standard electro-optical sampling to measure the THz transmission through a bare  $\text{NdGaO}_3$  reference substrate and the LCMO/NGO sample. By calculating the phase and amplitude information of the THz pulses in the frequency domain, the THz conductivity or photoinduced change in the conductivity can be measured.

**Single-shot measurement.** *Single-shot THz conductivity measurement.* The intracavity Pockels cell of the Ti:sapphire laser is disabled to stop the output of pulses at 1 kHz. To emit a single pulse a trigger signal is sent to enable the Pockels cell. In this way, a single laser pulse perturbs the sample. The subsequent THz conductivity measurement is performed after switching back to the 1 kHz output mode. This process is repeated on a shot-by-shot basis.

*Single-shot optical pump-probe spectroscopy.* Single-shot pump-probe spectroscopy was carried out using a dual-echelon single-shot instrument (Supplementary Fig. 5). A single pump pulse excites the sample while an array of probe pulses, generated by a pair of crossed echelons, probes the centre of the pump spot, reflects off the sample, and is imaged on a charge-coupled device (CCD) camera. This generates 400 probe pulses, spaced 23 fs apart. For each pump shot, two images of the echelons are recorded, a signal and background. The ratio of signal and background intensities is used to extract the single-shot pump-probe traces. The laser system is a 1 kHz Ti:sapphire regenerative amplifier system, downcounted using a Pockels cell/polarizer to 10 Hz, and further gated with shutters. The sample is pumped with a 70 fs, 800 nm pulse, and probed with the output of a non-collinear optical parametric amplifier (NOPA) tuned to 730 nm (1.7 eV) with a 50 fs pulse width.

*Single-shot optical image.* Single-shot optical images were taken simultaneously with single-shot optical pump-probe spectroscopy by imaging the white light source irradiated sample onto a CCD camera operating in the visible range.